Detecting Magnetic Fields in Exoplanets with Spectropolarimetry of the Helium Line at 1083 nm

Antonija Oklopčić[1,6] , Makana Silva[2,3] , Paulo Montero-Camacho[2,3,4] , and Christopher M. Hirata[2,3,5]

[1] Center for Astrophysics | Harvard & Smithsonian, 60 Garden Street, MS-16, Cambridge, MA 02138, USA; antonija.oklopcic@cfa.harvard.edu
[2] Center for Cosmology and AstroParticle Physics (CCAPP), The Ohio State University, Columbus, OH 43210, USA
[3] Department of Physics, The Ohio State University, 191 West Woodruff Avenue, Columbus, OH 43210, USA
[4] Department of Astronomy, Tsinghua Center for Astrophysics, Tsinghua University, Beijing 100084, People's Republic of China
[5] Department of Astronomy, The Ohio State University, 140 West 18th Avenue, Columbus, OH 43210, USA

Abstract

The magnetic fields of the solar system's planets provide valuable insights into their interiors and can have dramatic consequences for the evolution of their atmospheres and interaction with the solar wind. However, we have little direct knowledge of magnetic fields in exoplanets. Here we present a method for detecting magnetic fields in the atmospheres of close-in exoplanets based on spectropolarimetric transit observations at the wavelength of the helium line at 1083 nm. This methodology has been successfully applied for exploring magnetic fields in solar coronal filaments. Strong absorption signatures (transit depths on the order of a few percent) in the 1083 nm line have recently been observed for several close-in exoplanets. We show that in the conditions in these escaping atmospheres, metastable helium atoms should be optically pumped by the starlight and, for field strengths more than a few $\times 10^{-4}$ G, should align with the magnetic field. This results in linearly polarized absorption at 1083 nm that traces the field direction (the Hanle effect), which we explore by both analytic computation and the HAZEL numerical code. The linear polarization $\sqrt{Q^2 + U^2}/I$ ranges from $\sim 10^{-3}$ in optimistic cases down to a few $\times 10^{-5}$ for particularly unfavorable cases, with very weak dependence on field strength. The line-of-sight component of the field results in a slight circular polarization (the Zeeman effect), also reaching $V/I \sim$ few $\times 10^{-5}(B_{\parallel}/10 \, \text{G})$. We discuss the detectability of these signals with current (SPIRou) and future (Extremely Large Telescope) high-resolution infrared spectropolarimeters, and we briefly comment on possible sources of astrophysical contamination.

Unified Astronomy Thesaurus concepts: Exoplanet atmospheres (487); Magnetic fields (994); Spectropolarimetry (1973)

1. Introduction

One of the most important planetary properties is the presence or absence of a global magnetic field. Since the magnetic field dynamos rely on differential rotation or convection of an electrically conducting fluid in the planet's interior, detecting and measuring planetary magnetic fields is one of the few ways to obtain information about the structure, composition, and dynamics of planetary interiors. Furthermore, the presence of a global magnetic field—shielding the planet from impacts of high-energy particles in the stellar wind—can have important consequences for the extent and longevity of a planetary atmosphere and ultimately determine whether a planet is habitable or not.

It is still an open question whether magnetic field dynamos in planets, brown dwarfs, and stars all share the same physical origin. Magnetic field strengths on the order of a kilogauss have been detected in brown dwarfs and low-mass stars (e.g., Reiners & Basri 2007; Morin et al. 2010; Kao et al. 2018). Most planets and some satellites in the solar system have or had in their past a global magnetic field, with average magnetic field strengths at their surface up to ∼5 G (in the case of Jupiter; Schubert & Soderlund 2011). One of the main challenges for understanding planetary dynamos is the small sample of solar system planets. Measuring the properties of magnetic fields in exoplanets could expand that sample and

provide valuable insights into the origin of planetary magnetic fields and its importance for planetary evolution.

One of the most promising avenues for detecting magnetic fields in exoplanets is using the radio electron cyclotron maser emission (e.g., Hallinan et al. 2008). However, no direct detections of magnetic fields in exoplanets have been made so far (e.g., Murphy et al. 2015; Lazio et al. 2018). Indirect detection of magnetic fields in several hot Jupiters, obtained by modeling star–planet magnetic interaction and its effect on stellar chromospheric emission, has recently been reported by Cauley et al. (2019).

Magnetic fields in stars, including the Sun, can be directly observed by their effect on atoms and molecules in stellar atmospheres. By changing the structure of atomic and molecular energy levels, magnetic fields affect the spectral line profiles and polarization properties of stellar radiation (e.g., Landi Degl'Innocenti & Landolfi 2004). Most easily observable manifestations of magnetic fields arise from the Zeeman effect, which causes magnetic sublevels of a given atomic state to split in energy. As a result, the spectral line appears broadened or split into multiple components, which are polarized. By observing radiation polarization in sunspots, Hale (1908) was the first to infer the presence of a magnetic field on the Sun, and most of our current knowledge of stellar magnetism comes from Zeeman spectroscopy and spectropolarimetry (e.g., Donati & Landstreet 2009).

Polarization in spectral lines, however, can also be induced by anisotropic radiation pumping, which creates population imbalances between different atomic sublevels and hence linear

---

[6] NHFP Sagan Fellow.

polarization in the emergent radiation (e.g., Landi Degl'Innocenti & Landolfi 2004). In the presence of a magnetic field, this atomic-level polarization gets modified through the action of the Hanle effect (Hanle 1924). This effect is sensitive to much weaker magnetic fields compared to the Zeeman effect, and its diagnostic potential has been utilized by the solar physics community for many years (e.g., Leroy et al. 1977; Stenflo et al. 1998; Trujillo Bueno et al. 2002, 2005). Of particular interest is the paper by Trujillo Bueno et al. (2002), which shows that in prominences and filaments levitating in the solar corona, the metastable lower level of the He I 1083 nm triplet is significantly polarized by the anisotropic radiation from the underlying solar disk, and that a significant amount of linear polarization is produced by selective absorption processes (see also Trujillo Bueno & Asensio Ramos 2007). Interestingly, as pointed out by Trujillo Bueno et al. (2002), the mere detection of He I 1083 nm linear polarization when observing filaments at the solar disk center implies the presence of a magnetic field, inclined with respect to the line of sight, in the filament plasma.

Founded on the same physical principles, here we propose a similar method for detecting magnetic fields in exoplanets. The method is based on high-resolution transmission spectro-polarimetry in the helium absorption line at 1083 nm; it is applicable to transiting hot planets with extended or escaping atmospheres. Observing a linear polarization signal in this spectral line during an exoplanet transit could reveal the presence of a magnetic field in the planet's atmosphere. The method is sensitive to a broad range of magnetic field strengths, including the field strengths found in the solar system planets. This paper is structured as follows. In Section 2 we provide the basic background on the helium line at 1083 nm and the polarimetry of spectral lines in the presence of magnetic fields. In Section 3 we present an analytic calculation of the effect an external magnetic field has on the polarization of the helium line. In Section 4 we present the results of numerical calculations for different magnetic field strengths and geometries using the HAZEL code (Asensio Ramos et al. 2008). In Section 5 we examine the prospects for observing the calculated polarization signals and discuss possible sources of contamination, and in Section 6 we summarize our results.

2. Background

2.1. Helium Absorption Line at 1083 nm

The helium line triplet at 1083 nm has recently been established as a powerful new diagnostic of upper atmospheres of exoplanets. An absorption signature in this line produced by a transiting exoplanetary atmosphere is sensitive to the physical properties (i.e., gas temperature, density, composition) and the dynamics (i.e., winds and outflows) of the atmospheric layers extending to distances of a few planetary radii, that is, the thermosphere and exosphere (Oklopčić & Hirata 2018). Studying this region of the atmosphere, close to the planet's Roche radius, is important for understanding the process of atmospheric escape and its effect on planetary evolution.

Helium absorption at 1083 nm was first detected in transit spectroscopy of WASP-107b by Spake et al. (2018), using the low-resolution data from the *Hubble Space Telescope*/Wide Field Camera 3. Since then, spectrally resolved absorption signatures of helium have been obtained for several exoplanets (HAT-P-11b, WASP-69b, HD 189733b, WASP-107b, HD 209458b) using
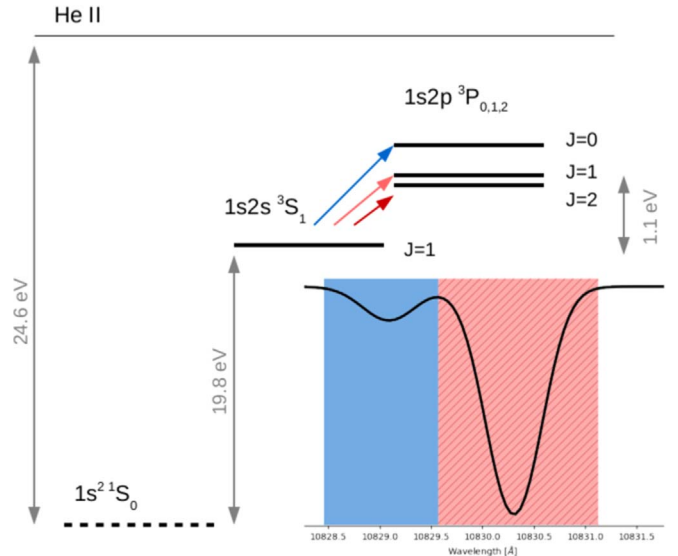

Figure 1. Schematic representation of atomic levels involved in the helium 1083 nm transitions (solid lines). The transition between the metastable (2^3S) level and the $J = 0$ level of 2^3P produces the "blue component" of the 1083 nm absorption line triplet, whereas the other two transitions blend together to form the "red component." Energy separations are not drawn to scale.

high-resolution ground-based observations (Allart et al. 2018, 2019; Nortmann et al. 2018; Salz et al. 2018; Alonso-Floriano et al. 2019).

The absorption triplet at 1083 nm originates from an excited 2^3S$_1$ level of the neutral helium atom in the triplet configuration. This level has only highly forbidden decays to the helium ground state (1^1S$_0$), and hence it is metastable, allowing a significant population of helium atoms in this excited level to build up in planetary thermospheres and exospheres. The upper level of the 1083 nm transition (2^3P$_{2,1,0}$) is split by fine structure into three levels with quantum numbers $J = 2$, $J = 1$, and $J = 0$. These three levels correspond to lines with wavelengths (in air) of 1083.034 nm, 1083.025 nm, and 1082.909 nm, respectively (Kramida et al. 2018). The first two are practically indistinguishable, and we refer to them jointly as the "red component," whereas the third, the "blue component," is usually separated. A schematic representation of the atomic transitions relevant for the helium 1083 nm line triplet and the line components they produce is given in Figure 1.

2.2. Polarization of Absorption Lines in the Presence of a Magnetic Field

We now review how atoms placed in a magnetic field and subject to an incident radiation field can become aligned[7] with the field and exhibit polarization-selective absorption. The setup is shown in Figure 2. This effect is well studied in the context of solar physics (see Trujillo Bueno & Landi Degl'Innocenti 1997; Trujillo Bueno et al. 2002), and here we will argue that all the circumstances required for a spectral line to be a useful probe of magnetic fields are satisfied by the He I 1083 nm triplet in extended exoplanet atmospheres around

---

7 Atoms are aligned with the magnetic field if the distribution of their spins is anisotropic but approximately axisymmetric around the field. Quantum mechanically, this means the density matrix is not proportional to the identity, but is approximately diagonal in the $|M_J\rangle$ basis with the z-axis along the field.
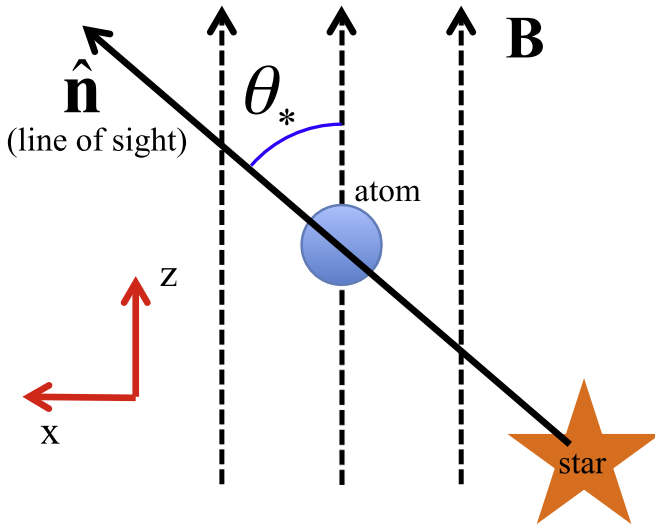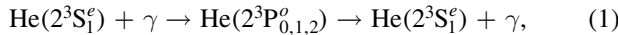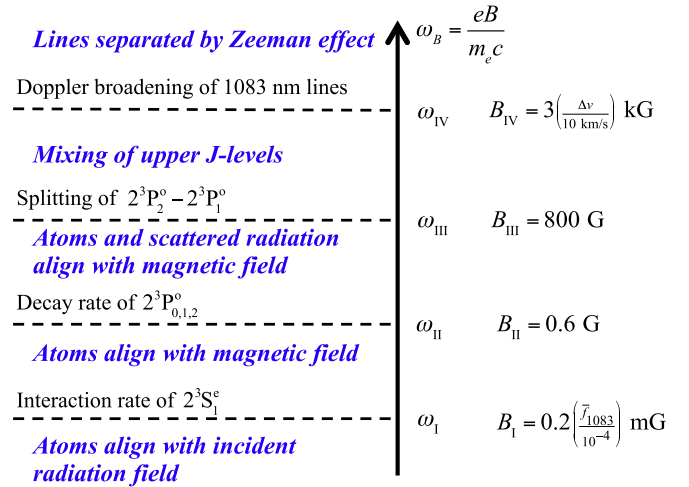
Figure 2. Setup for Section 2.2.

Figure 3. Different regimes of magnetic field strength relevant to the He I 1083 nm triplet. At very low field strength, $B < B_I$, the precession rate is less than the interaction rate of He I 2^3S, and the magnetic field is only a small perturbation on the alignment of the atoms. When $B > B_I$, the precession rate is fast, and the metastable helium atoms have an axisymmetric spin distribution around the magnetic field. At even higher fields, $B > B_{II}$, the precession rate is faster than the decay rate of 2^3P, and the scattered 1083 nm photons (emitted when the atoms decay back to 2^3S) are also axisymmetric around $\boldsymbol{B}$. At $B > B_{III}$, the precession rate exceeds the spin–orbit splitting $2^3P^o_2$–$2^3P^o_1$, and the upper J-levels are mixed. Finally, at very large fields, $B > B_{IV}$, the Zeeman splitting exceeds the Doppler width of the line, and the components of different polarization are separated. Note B_{II} and B_{III} are fixed by atomic physics, but B_I and B_{IV} depend on the environment; we show representative values. The treatment in Section 3 assumes $B_I < B < B_{III}$.

late-type stars (with the possible exception of the magnetic field strength, which is not known at present, and which we hope to constrain). Along the way, we will discuss the relevant field strengths, both in terms of B and in terms of the cyclotron frequency $\omega_B = eB/m_ec$, which to an order of magnitude is the precession frequency of an atom in a magnetic field.[8] Key field strengths where there is a qualitative change in behavior, B_I, B_{II}, B_{III}, and B_{IV}, are shown in Figure 3.

The first requirement is that the lower level of the transition have a nonzero angular momentum J_l so that there is something to align. If we want linearly polarized absorption, the atom must be able to have a spin 2 component of the density matrix (since Q and U have spin 2), so this requires $J_l \geqslant 1$ by the triangle inequality. This is the case for the level $2^3S^e_1$, which has $J_l = 1$.

Second, absorption of radiation followed by emission must be able to align the atoms; that is, in the scattering process

$$\mathrm{He}(2^3\mathrm{S}^e_1) + \gamma \rightarrow \mathrm{He}(2^3\mathrm{P}^o_{0,1,2}) \rightarrow \mathrm{He}(2^3\mathrm{S}^e_1) + \gamma, \qquad (1)$$

we must be able to start from an initial random state ($M_J = -1$, 0, or $+1$ equally likely) and leave the atom in a nonrandom final state. Here in the absorption step, the angular momentum of the photon is transferred to the orbital angular momentum of the electrons, and in the emission step the orbital angular momentum of the electrons is transferred to the outgoing photon. If there were no spin–orbit coupling, then the total electron spin would be conserved through this whole process, and the final M_J would equal the initial M_J. However, the fine structure splittings of the He I $2^3P^o_{0,1,2}$ levels are large compared to their intrinsic width, which means that the total electron spin S is *not* conserved; rather, in the intermediate state, the spin and orbital angular momenta can precess around each other for many cycles before the atom decays back to $2^3S^e_1$. Therefore, the final spin of the atom will have some dependence on the angular momentum of the incident photon. Since most incident photons come from the star and

carry angular momentum $\pm\hbar$ (but not zero) projected along the line-of-sight ($\hat{\boldsymbol{n}}$) direction, this final spin is not random. The distribution of final states will depend on the angle $\theta_\star$ between the line of sight and the magnetic field. If the field strength is small enough to ignore Zeeman splittings (see below), then the alignment of atoms will be of the quadrupole or "headless vector" nature; that is, the $M_J = -1$ and $M_J = +1$ final states are equally likely, but their probability will differ from $M_J = 0$.

Third, the atoms must precess around the magnetic field fast enough that they align with the field and not with the direction of incident radiation (in the latter case—the *zero-field case*, according to the terminology used in Landi Degl'Innocenti & Landolfi 2004—we know from symmetry considerations that they will produce no polarization). This means that the precession rate $\sim\omega_B$ must be large compared to the rate at which the atoms scatter photons, $3A_{ul}\bar{f}_{1083}$, where 3 is a ratio of statistical weights and $\bar{f}_{1083}$ is the isotropically averaged phase space density of photons in the 1083 nm line.[9] This requirement implies $B > B_I = 0.2(\bar{f}_{1083}/10^{-4})$ mG, where $\bar{f}_{1083}$ is typically of order 10^{-4} near hot exoplanets. This is the lower-level Hanle effect regime.

Fourth, the atoms in the lower level must not be depolarized or depopulated by other interactions. This means that the scattering rate $3A_{ul}\bar{f}_{1083}$ in the 1083 nm triplet must be large compared to the rate of spontaneous decay A_l, collisions $\sum_i n_i\langle\sigma v\rangle_i$ (including all available projectiles i), and photoionization Φ_l. Here we are helped by the metastable nature of the $2^3S^e_1$ level (small A_l), the high radiation flux and low gas density in the escaping atmospheres (see the Appendix), and

---

[8] The precession frequency of an atom is $\omega_{\mathrm{prec}} = \frac{g_J}{2}\omega_B$, where g_J is the Landé g-factor. Standard formulae (e.g., Rybicki & Lightman 1979, Equation (9.35b)) give $\frac{g_J}{2} = 1$ for 2^3S and $\frac{g_J}{2} = \frac{3}{4}$ for 2^3P.

[9] This is related to the isotropically averaged specific intensity by $J_\nu = (2h\nu^3/c^2)\bar{f}_{1083}$.

the red spectrum of the K-type stars hosting He I detections, which results in a much higher rate for 1083 nm scattering than photoionization from the $2^3S_1^e$ level (requiring $\lambda < 260$ nm photons). A review of most of these rates can be found in Section 3.3 of Oklopčić & Hirata (2018) and in Figure 4 of Oklopčić (2019).

Finally, it is not enough to align the spins of the atoms; we must also have a spectral diagnostic that is sensitive to this alignment. The key to this is the fine structure splitting: the cross section for $2^3S_1^e$–$2^3P_J^o$ for a given final J depends on the relative orientations of the initial spin of the atom and the polarization of the incoming light. This is simplest to understand for the absorption line leading to the $J = 0$ upper level, which always has $M_J = 0$. The transition obeys a selection rule in which the E_z component of the incident electric field (which preserves symmetry around the z-axis) must lead to $\Delta M_J = 0$ by conservation of angular momentum, whereas the E_x and E_y components lead to $\Delta M_J = \pm 1$. Thus the $M_J = 0$ initial state only absorbs light in the $2^3S_1^e$–$2^3P_0^o$ line for the vertical polarization (see Figure 2), whereas the $M_J = \pm 1$ initial states can absorb light in the horizontal polarization as well (at $\theta_\star = \pi/2$, this must be horizontal, but in general it may be either vertical or horizontal). Similar but more complicated considerations apply to the $J = 1$ and $J = 2$ upper levels. This means that the "headless vector" alignment of helium atoms—where $M_J = 0$ has a different occupation from $M_J = \pm 1$—should produce linearly polarized absorption.

At high field strengths, other effects begin to occur. For $B > B_{II}$ (see Figure 3) or $\omega_B > A_{ul}$, the excited He I 2^3P atoms can precess before they decay (i.e., the upper-level Hanle effect); in this case, the scattered radiation will be randomized in longitude around the magnetic field. However, because in transits we observe absorption and not primarily the scattered light, this should have only a minor influence on the observed transit depth. At $B > B_{III}$ or $\omega_B > \Delta E(2^3P_2^o - 2^3P_1^o)/\hbar$, there is mixing of the upper J-levels; this changes the calculation of the optical pumping, but the alignment mechanism still works. At very high magnetic field strengths (i.e., in the *intense field regime*), there will be a Zeeman splitting of the 1083 nm line components that can result in circular polarization. The lines become separated for $\omega_B > \omega_0(\Delta v/c)$ or $B > B_{IV} = 3(\Delta v/10 \text{ km s}^{-1})$ kG, where $\omega_0 = 1.74 \times 10^{15}$ s^{-1} is the angular frequency of the line. Even for smaller field strengths—in the so-called *intermediate regime* —one expects the line components with different circular polarization to be slightly separated, such that Stokes V has a negative–positive pattern around each line. We do not consider this in our simplified analytic calculation in Section 3, but it is included in the numerical calculations of Section 4 using HAZEL.

3. Simplified Analytic Calculation

In this section, we will go through a simplified calculation for obtaining the optical depth and Stokes parameters Q and I for transmitted radiation from metastable helium atoms in a magnetic field that are pumped by incident starlight. In Section 3.1, we state our underlying assumptions. We set up the optical pumping calculation in Section 3.2 and solve the resulting equations for the atomic density matrix in Section 3.3. We arrive at the analytic results for polarization-selective absorption in Section 3.4.

3.1. Assumptions, Range of Validity, and Notation

In order to calculate an analytic solution to this problem, we first establish our assumptions about the system of interest. We first simplify the problem by assuming a uniform magnetic field and a small optical depth (so that the probability of multiple scattering in the 1083 nm line is small). These approximations are purely to simplify the problem and estimate the order of magnitude of the signal strength. For example, inhomogeneous magnetic fields could be modeled by superposing several field geometries; scattered light adds complexity and can be treated with numerical codes as in Section 4, but does not change the essential aspects of the problem.

In treating the pumping of the metastable helium atoms by the ambient 1083 nm radiation field, we work in the case where the angular size of the star is negligible (so that $\cos\theta$ does not vary over the star's disk, and we can set $\theta \approx \theta_\star$ for incoming radiation) and the emitted light is of a smooth spectrum and unpolarized. This is justified in that the planet is many stellar radii from the star, and the stellar He I 1083 nm lines are weaker than the continuum. Similarly, if we are at least a couple planetary radii from the planet, we neglect 1083 nm photons from the star that reflect off the planet.

The next assumption is the range of the magnetic field strength. As stated in Section 2.2, we want a magnetic field with strength great enough to allow for fast precession of the atom but not strong enough to mix the J-levels in $2^3P_{2,1,0}^o$. This puts $B_{min} \approx B_I = 0.2$ mG and $B_{max} \approx B_{III} = 800$ G. Fast precession guarantees that the density matrix of metastable helium He I $2^3S_1^e$ is diagonal in the M_J basis.

When describing states, we will use capital letters N, R, T, and W to denote states in the $2^3S_1^e$ metastable level and Greek letters μ and ν to denote states in the $2^3P_{2,1,0}^o$ excited levels. Components of vectors will be written with lowercase letters. Quantum numbers of these states will be written with the state as a subscript, such as in J_μ and $M_{J,\mu}$, where J and M_J follow standard atomic physics notation.

3.2. Polarization of the Metastable Helium Atoms: Setup

In order to compare the analytic solution to the results of the HAZEL code, we will want to compute the polarization of the transmitted light under the presence of a uniform magnetic field. Our first step is to calculate the density matrix of the metastable He I atoms. This is a 3×3 Hermitian matrix, with trace equal to 1. We want to find steady-state solutions to the density matrix evolution equation for helium atoms in the $2^3S_1^e$ level:

$$\dot{\rho}_{B,TW} + \dot{\rho}_{depop,TW} + \dot{\rho}_{repop,TW} = 0. \tag{2}$$

The first term is given by the Zeeman splitting of states T and W:

$$\dot{\rho}_{B,TW} = i\frac{g_l}{2}\omega_B(M_{J,W} - M_{J,T})\rho_{TW}, \tag{3}$$

where the Landé g-factor for the lower level is $g_l = 2$. The second term has the form

$$\dot{\rho}_{depop,TW} = -\frac{3}{4\pi}A_{ul}f_{star}(\omega_0)\Omega_{star}\rho_{TW}, \tag{4}$$

where A_{ul} is the Einstein coefficient for spontaneous emission, and $f_{star}(\omega)$ and Ω_{star} are the phase space of incoming photons

from the star and the solid angle of the star as seen by the atom, respectively. (The angular average phase space density is $\bar{f}_{1083} = f_{\text{star}}(\omega_0) \times \Omega_{\text{star}}/4\pi$.) The first term in Equation (2) represents precession of He atoms around the magnetic field; the second term represents the absorption of 1083 nm photons ("depopulation" from the initial level); and the third term represents atoms that have absorbed 1083 nm photons, but then re-emit a photon and return to the $2^3S_1^e$ level ("repopulation" into the initial level).

In order to accurately describe the population of the different relevant states (i.e., solve Equation (2)), we are only missing the repopulation term. We begin our analysis with the time evolution of the repopulation density matrix in

$$C_{qs}\left(\hat{\boldsymbol{k}}_\gamma\right) \equiv \sum_{\alpha=H,V} (\boldsymbol{e}_\alpha(\hat{\boldsymbol{k}}_\gamma))_q (\boldsymbol{e}_\alpha^*(\hat{\boldsymbol{k}}_\gamma))_s = \begin{pmatrix} -\frac{1}{2}e^{2i\phi}\sin^2\theta & -\frac{1}{\sqrt{2}}e^{i\phi}\cos\theta\sin\theta & -\frac{1}{2}(1+\cos^2\theta) \\ -\frac{1}{\sqrt{2}}e^{i\phi}\cos\theta\sin\theta & \sin^2\theta & \frac{1}{\sqrt{2}}e^{-i\phi}\cos\theta\sin\theta \\ -\frac{1}{2}(1+\cos^2\theta) & \frac{1}{\sqrt{2}}e^{-i\phi}\cos\theta\sin\theta & -\frac{1}{2}e^{-2i\phi}\sin^2\theta \end{pmatrix} = g_{qs} - \hat{k}_q \hat{k}_s, \quad (6)$$

Equation (51) of Venumadhav et al. 2017 (see also Equations III,10 and III,11 of Barrat & Cohen-Tannoudji 1961 for a similar derivation):

$$\dot{\rho}_{\text{repop,TW}} = \int \frac{d^3\boldsymbol{k}_\gamma}{(2\pi)^3}\frac{d^3\boldsymbol{k}_\gamma'}{(2\pi)^3}\sum_{\alpha,\beta,\mu,N,\nu,R}\hbar^{-4}(2\pi\hbar)^2\omega\omega'f(\boldsymbol{k}_\gamma)$$

$$\times \langle T|\boldsymbol{d}\cdot e_\beta^*(\hat{\boldsymbol{k}}_\gamma')|\mu\rangle\langle\mu|\boldsymbol{d}\cdot e_\alpha(\hat{\boldsymbol{k}}_\gamma)|N\rangle$$

$$\times \langle\nu|\boldsymbol{d}\cdot e_\beta(\hat{\boldsymbol{k}}_\gamma')|W\rangle\langle R|\boldsymbol{d}\cdot e_\alpha^*(\hat{\boldsymbol{k}}_\gamma)|\nu\rangle$$

$$\times \frac{\rho_{\text{NR}}\pi\delta(\omega'-\omega+\omega_{\text{WR}})}{[(\omega-\omega_{\mu N})+i\Gamma_{2^3\text{P}}/2][(\omega-\omega_{\nu R})-i\Gamma_{2^3\text{P}}/2]}$$

$$+ \text{h.c.},$$

$$(5)$$

where $\boldsymbol{k}_\gamma$, $\boldsymbol{k}_\gamma'$, and $\boldsymbol{d}$ represent the incoming and outgoing photon momentum and the dipole moment operator, respectively. The $e_{\alpha(\beta)}(\hat{\boldsymbol{k}}('){}_\gamma)$ are the polarization unit vectors of incoming (outgoing) radiation. The indices α and β run over the polarization states of the incoming and outgoing radiation, respectively. The remaining indices run over the possible initial states (N, R) and intermediate states (μ, ν) of the atom. The width of the intermediate states is $\Gamma_{2^3\text{P}}$. The "h.c." stands for Hermitian conjugate. Equation (5) is essentially the density matrix version of Fermi's Golden Rule for second-order transitions. Physically, it describes the evolution of the ground state taking into account the absorption of a 1083 nm photon ($\boldsymbol{k}_\gamma$) from the ground state to an excited state followed by the subsequent emission of a 1083 nm photon ($\boldsymbol{k}_\gamma'$). The matrix element for this process contains the dipole matrix element to excite the atom ($N \rightarrow \mu$), a propagator (denominator $\omega - \omega_{\mu N} + i\Gamma_{2^3\text{P}}/2$), and the dipole matrix element for de-excitation ($\mu \rightarrow T$). The density matrix formulation has two copies of this matrix element (for $N \rightarrow T$ and $R \rightarrow W$) rather than a matrix element squared. There is an integral over the phase space for ingoing and outgoing photons ($\int d^3k/(2\pi)^3$ and $\int d^3k'/(2\pi)^3$, respectively), polarization sums (over α and β), and a phase space density for ingoing photons.

The factor $\pi\delta(\omega'-\omega+\omega_{\text{WR}})$ + h.c. is the usual energy-conserving δ-function or density of states.

We can further simplify Equation (5) by expanding the dot products in the matrix elements into their components and performing the sum over polarization states. For convenience when working with angular momentum coupling, we work in the spherical basis, where the basis vectors are $\hat{\boldsymbol{e}}_0 = \hat{\boldsymbol{e}}_z$ and $\hat{\boldsymbol{e}}_\pm 1 = \mp\frac{1}{\sqrt{2}}(\hat{\boldsymbol{e}}_x \pm i\hat{\boldsymbol{e}}_y)$. In this basis, the dot product of two vectors can be written as $\boldsymbol{a}\cdot\boldsymbol{b} = \sum_{qs} g_{qs}a_q b_s$, where the metric tensor $g_{qs} = (-1)^q\delta_{qs}$. Note, however, that in a complex basis we must distinguish between the complex conjugate of a vector component $(a_q)^*$ and a component of a complex conjugate $(a^*)_q$. The sum over polarization states is the tensor

where H and V represent the horizontal and vertical polarization states, and q and s are the components of the unit vectors that span the range -1, 0, and $+1$ (spherical basis, written in that order). A similar tensor is also defined for the outgoing radiation. With this replacement, we see that

$$\sum_{\alpha=H,V}(\boldsymbol{a}\cdot\boldsymbol{e}_\alpha(\hat{\boldsymbol{k}}_\gamma))(\boldsymbol{b}\cdot\boldsymbol{e}_\alpha^*(\hat{\boldsymbol{k}}_\gamma)) = \sum_{q,s}(-1)^q(-1)^s a_q b_s C_{-q,-s}$$

$$= \sum_{q,s} a_q b_s [C_{qs}(\hat{\boldsymbol{k}}_\gamma)]^*.$$

$$(7)$$

Note the useful fact that the integral over all directions is $\int_{S^2} C_{qs}(\hat{\boldsymbol{k}}_\gamma)d^2\hat{\boldsymbol{k}}_\gamma = \frac{8\pi}{3}g_{qs}$.

The integrals over photon momentum can be rewritten in spherical coordinates: $\int_0^\infty dk \int_{S^2} d^2\hat{\boldsymbol{k}}\, k^2/(2\pi)^3$. We can simplify Equation (5) by integrating it over incoming and outgoing photon solid angles to get

$$\dot{\rho}_{\text{repop,TW}} = \sum_{\mu,N,\nu,R,q,s,n,r}\int\frac{dk_\gamma\, k_\gamma^2}{(2\pi)^3}\frac{dk_\gamma'\, k_\gamma'^2}{(2\pi)^3}\hbar^{-4}(2\pi\hbar)^2\omega\omega'$$

$$\times \frac{8\pi^2}{3}(-1)^n\delta_{n,-r}f_{\text{star}}(\omega)[C_{qs}(\hat{\boldsymbol{n}})]^*\Omega_{\text{star}}$$

$$\times \langle T|d^n|\mu\rangle\langle\mu|d^q|N\rangle\langle\nu|d^r|W\rangle\langle R|d^s|\nu\rangle$$

$$\times \frac{\rho_{\text{NR}}\delta(\omega'-\omega+\omega_{\text{WR}})}{[(\omega-\omega_{\mu N})+i\Gamma_{2^3\text{P}}/2][(\omega-\omega_{\nu R})-i\Gamma_{2^3\text{P}}/2]}$$

$$+ \text{h.c.},$$

$$(8)$$

where $C_{qs}(\hat{\boldsymbol{n}})$ is Equation (6) evaluated for the direction of incident starlight.

In order to further simplify Equation (8), we need to use the assumption that the spectrum of incoming radiation is smooth and unpolarized. We convert the wavenumber integrals to frequency using $k_\gamma = \omega/c$ and $k_\gamma' = \omega'/c$. Thus we can pull the phase space density of incident photons and all smoothly varying functions of ω out of the integral, and integrate over k_γ'

(using the δ function) and k_γ (using contour integration) to get

$$\dot{\rho}_{\text{repop,TW}} = \sum_{\mu,N,\nu,R,q,s,n,r} \hbar^{-4} \frac{(2\pi\hbar)^2}{(2\pi c)^6}$$
$$\times \frac{8\pi^2}{3}(-1)^n \delta_{n,-r}[C_{qs}(\hat{\boldsymbol{n}})]^* \Omega_{\text{star}}$$
$$\times \langle T|d^n|\mu\rangle\langle\mu|d^q|N\rangle\langle\nu|d^r|W\rangle\langle R|d^s|\nu\rangle$$
$$\times \frac{2\pi i \rho_{\text{NR}} f(\omega_0)\omega_0^6}{\omega_{\nu R} - \omega_{\mu N} + i\Gamma_{2^3\text{P}}} + \text{h.c.} , \quad (9)$$

where again $\omega_0 = 1.74 \times 10^{15}$ s^{-1} is the line transition frequency (used only in places where there is a negligible difference depending on which of the three lines is used). To simplify the matrix elements appearing in Equation (9), we will use the Wigner–Eckart theorem and the formula for double-barred matrix elements in spin–orbit coupling (see Equation (7.1.7) of Edmonds 1960) to find

$$D_{\mu T}^n \equiv \langle\mu|d^n|T\rangle$$
$$= (-1)^{J_\mu - M_{J,\mu} + L_\mu + S_\mu + J_T + 1}\sqrt{(2J_\mu + 1)(2J_T + 1)}$$
$$\times \begin{pmatrix} J_\mu & 1 & J_T \\ -M_{J,\mu} & n & M_{J,T} \end{pmatrix}\begin{Bmatrix} L_\mu & J_\mu & S_\mu \\ J_T & L_T & 1 \end{Bmatrix}$$
$$\times \langle n_\mu, L_\mu||\boldsymbol{d}||n_T, L_T\rangle$$
$$= (-1)^{M_{J,\mu}}\sqrt{\frac{2J_\mu + 1}{3}}\begin{pmatrix} J_\mu & 1 & 1 \\ -M_{J,\mu} & n & M_{J,T} \end{pmatrix}\langle 2^3\text{P}^o||\boldsymbol{d}||2^3\text{S}^e\rangle.$$
$$(10)$$

In the second step, we used the fact that $S_\mu = S_T = 1$, $L_T = 0$, $L_\mu = 1$, and $J_T = 1$ to simplify the phase factors and $6j$ symbols. The final double-barred matrix element acts on the orbital wave function only. Note that the matrix element going the other way is $\langle T|d^n|\mu\rangle = (-1)^n(D_{\mu T}^{-n})^*$ because $(d^n)^\dagger = (-1)^n d^{-n}$. We then obtain

$$\dot{\rho}_{\text{repop,TW}} = \sum_{\mu,N,\nu,R,q,s,n,r} \hbar^{-4} \frac{(2\pi\hbar)^2}{(2\pi c)^6}\frac{8\pi^2}{3}(-1)^{2n+s}\delta_{n,-r}$$
$$\times [C_{qs}(\hat{\boldsymbol{n}})]^* \Omega_{\text{star}}(D_{\mu T}^{-n})^* D_{\mu N}^q D_{\nu W}^r (D_{\nu R}^{-s})^*$$
$$\times \frac{2\pi i \rho_{\text{NR}} f_{\text{star}}(\omega_0)\omega_0^6}{\omega_{\nu R} - \omega_{\mu N} + i\Gamma_{2^3\text{P}}}$$
$$+ \text{h.c.} . \quad (11)$$

3.3. Polarization of the Metastable Helium Atoms: Solution

Equation (2), with Equations (3), (4), and (11) describing the terms, completely specifies the density matrix evolution and can be used to solve for the steady-state solution. While we could solve for the full general density matrix, the fast precession assumption (Section 3.1) will allow us to simplify the result. The $\dot{\rho}_{\text{TW}}$ term can be written as

$$(i\omega_B(M_{J,W} - M_{J,T}) - 3A_{\text{ul}}\bar{f}_{1083})\rho_{\text{TW}} + \dot{\rho}_{\text{repop,TW}}$$
$$= 0 \rightarrow \rho_{\text{TW}} = \frac{\dot{\rho}_{\text{repop,TW}}}{3A_{\text{ul}}\bar{f}_{1083} - i\omega_B(M_{J,W} - M_{J,T})}. \quad (12)$$

For $T = W$, the denominator is simply $3A_{\text{ul}}\bar{f}_{1083}$, and by adding the three possible states of T, we get $1 = \text{Tr}\,\rho = \text{Tr}\,\dot{\rho}_{\text{repop}}/(3A_{\text{ul}}\bar{f}_{1083})$. For $T \neq W$, the absolute value of the denominator is at least ω_B (since $M_{J,W} - M_{J,T}$ is a nonzero integer). Thus we find

$$|\rho_{\text{TW}}| \leqslant \frac{\text{Tr}\,\dot{\rho}_{\text{repop}}}{\omega_B} = \frac{3A_{\text{ul}}\bar{f}_{1083}}{\omega_B}$$
$$= \frac{B_{\text{I}}}{B} \ll 1 \quad \text{for} \quad T \neq W \text{ and } B \gg B_{\text{I}}. \quad (13)$$

That is, in our "fast precession" approximation, the off-diagonal terms in the density matrix are small compared to 1, and we drop them in what follows.

We can further simplify Equation (11) by expanding the matrix elements using Equation (10) and utilizing the assumptions stated in Section 3.1 (mainly fast precession) in order to obtain

$$\dot{\rho}_{\text{repop,TT}} = \sum_{J_\mu=0}^2 \sum_{M_{J,\mu}=-J_\mu}^{J_\mu} \sum_{M_{J,N}=-1}^1$$
$$\times \frac{\Omega_{\text{star}}\omega_0^6 f_{\text{star}}(\omega_0)\rho_{\text{NN}}}{3\pi\hbar^2 c^6 \Gamma_{2^3\text{P}}}(-1)^{M_{J,N} - M_{J,\mu}}$$
$$\times [C_{M_{J,\mu} - M_{J,N}, M_{J,N} - M_{J,\mu}}(\hat{\boldsymbol{n}})]^* \frac{(2J_\mu + 1)^2}{9}$$
$$\times |\langle 2^3\text{P}^o||\boldsymbol{d}||2^3\text{S}^e\rangle|^4 \begin{pmatrix} J_\mu & 1 & 1 \\ -M_{J,\mu} & M_{J,\mu} - M_{J,T} & M_{J,T} \end{pmatrix}^2$$
$$\times \begin{pmatrix} J_\mu & 1 & 1 \\ -M_{J,\mu} & M_{J,\mu} - M_{J,N} & M_{J,N} \end{pmatrix}^2 + \text{h.c.} . \quad (14)$$

We can also work in the approximation that $\Gamma_{2^3\text{P}} \approx A_{2^3\text{P}^o \rightarrow 2^3\text{S}^e}$ because we are assuming that the atoms are far enough from the star that the incident radiation is not strong enough to stimulate emission of radiation (mean occupation number $\ll 1$, so spontaneous emission dominates). Simplifying Equation (14) with this approximation and using the dipole emission formula

$$A_{2^3\text{P}^o \rightarrow 2^3\text{S}^e} = \frac{4\omega_0^3}{9\hbar c^3}|\langle 2^3\text{P}^o||\boldsymbol{d}||2^3\text{S}^e\rangle|^2, \quad (15)$$

and using appropriate trigonometric identities, we get

$$\dot{\rho}_{\text{repop,TT}} = \frac{3\tilde{A}}{4\pi}M_{\text{repop,TN}}\rho_{\text{NN}} , \quad (16)$$

where we introduce

$$\tilde{A} \equiv \Omega_{\text{star}}f_{\text{star}}(\omega_0)A_{2^3\text{P}^o \rightarrow 2^3\text{S}^e} \quad \text{and} \quad \boldsymbol{M}_{\text{repop}}$$
$$= \frac{1}{144}\begin{pmatrix} 93 + 7\cos 2\theta_\star & 35 + \cos 2\theta_\star & 21 + 7\cos 2\theta_\star \\ 30 - 14\cos 2\theta_\star & 74 - 2\cos 2\theta_\star & 30 - 14\cos 2\theta_\star \\ 21 + 7\cos 2\theta_\star & 35 + \cos 2\theta_\star & 93 + 7\cos 2\theta_\star \end{pmatrix}. \quad (17)$$

For the diagonal elements of the density matrix, the first term in Equation (2) will go to zero. This simplifies Equation (2) to

$$(\boldsymbol{M}_{\text{repop}} - \mathbb{1})\rho_{\text{TT}} = 0 . \quad (18)$$

Physically, $\boldsymbol{M}_{\text{repop}}$ is a matrix of transition probabilities from one state to another, so $\boldsymbol{M}_{\text{repop}}$ has a single eigenvalue that is
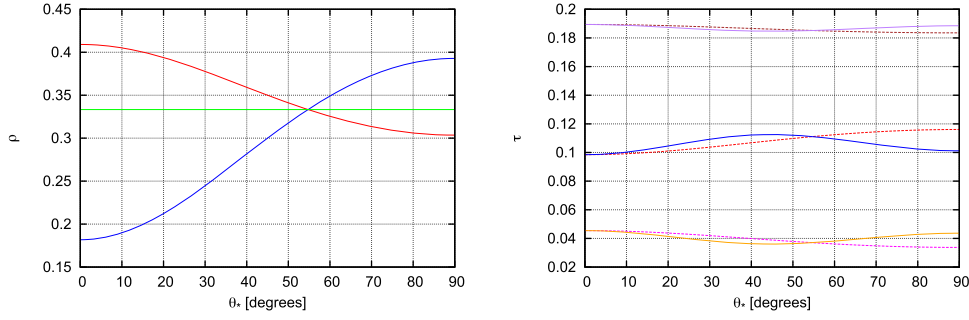
Figure 4. Left panel: the blue curve is a plot of ρ_{-1-1} and ρ_{11}, and red is the ρ_{00} as a function of the direction of incident radiation. The green constant line is the symmetric average of each component, that is, $\frac{1}{3}$. Right panel: This is a plot of the $\tau_{(H,V)}^{J_f}$ as a function of incident radiation. The lowest two curves (magenta and orange) are $\tau_{(H,V)}^0$, the middle curves (red and blue) are $\tau_{(H,V)}^1$, and the top two curves (brown and purple) are $\tau_{(H,V)}^2$ (we use the solid line for the vertical polarization and the dashed line for horizontal polarization).
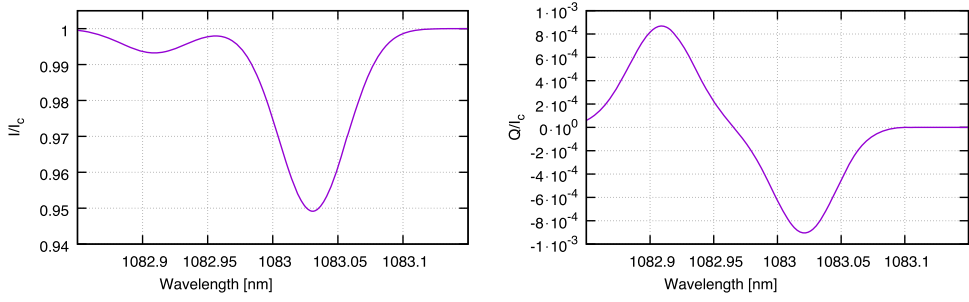
Figure 5. Left panel: analytic solution for total intensity (I/I_c). Right panel: analytic solution for the linear polarization Stokes parameter Q/I_c for a magnetic field perpendicular to the line of sight, $\theta_\star = \frac{\pi}{2}$.

equal to 1 because we care about steady-state solutions. This means all solutions to Equation (18) are proportional to the corresponding eigenvector. We can set the normalization by requiring $\mathrm{Tr}\,\rho = 1$, that is, total probability unity. This gives the components of ρ_{TT} as

$$\rho_{\mathrm{TT}} = \left(\frac{35 + \cos 2\theta_\star}{100 - 12\cos 2\theta_\star}, \frac{15 - 7\cos 2\theta_\star}{50 - 6\cos 2\theta_\star}, \frac{35 + \cos 2\theta_\star}{100 - 12\cos 2\theta_\star} \right). \quad (19)$$

The left panel of Figure 4 shows the population of atoms in the $2^3S_1^e$ state from the different states within $2^3P_{0,1,2}^o$ as a function of incoming radiation.

3.4. Polarization-selective Absorption in the 1083 nm Triplet

Finally, we have the required ingredients to compute the absorption optical depth for horizontally—and vertically—polarized light. The optical depth at line center is given by

$$\tau_{(H,V)}^{J_f} \propto \sum_{M_{J_f}, M_J} |\langle 2^3P_{J_f}^o, M_{J_f} | \boldsymbol{d} \cdot \boldsymbol{e}_{(H,V)} | 2^3S^e, M_J \rangle|^2$$
$$\times \rho_{M_J M_J}, \quad (20)$$

where J_f is the total angular momentum of the final state (0, 1, or 2), and $e_{(H,V)}$ are the unit polarization vectors for horizontal and vertical light, respectively. The normalization factor depends on the metastable helium column density and velocity dispersion. The functional forms of Equation (20) as a function

of $\theta_\star$ are

$$\tau_H^0 \propto \frac{35 + \cos 2\theta_\star}{36(25 - 3\cos 2\theta_\star)}, \quad (21)$$

$$\tau_V^0 \propto \frac{65 - 8\cos 2\theta_\star + 15\cos^2 2\theta_\star}{72(25 - 3\cos 2\theta_\star)}, \quad (22)$$

$$\tau_H^1 \propto \frac{13(5 - \cos 2\theta_\star)}{24(25 - 3\cos 2\theta_\star)}, \quad (23)$$

$$\tau_V^1 \propto \frac{135 - 16\cos 2\theta_\star - 15\cos^2 2\theta_\star}{48(25 - 3\cos 2\theta_\star)}, \quad (24)$$

$$\tau_H^2 \propto \frac{5(67 - 7\cos 2\theta_\star)}{72(25 - 3\cos 2\theta_\star)}, \quad \text{and} \quad (25)$$

$$\tau_V^2 \propto \frac{5(133 - 16\cos 2\theta_\star + 3\cos^2 2\theta_\star)}{144(25 - 3\cos 2\theta_\star)}. \quad (26)$$

The right panel of Figure 4 shows the plot of $\tau_{(H,V)}^{J_f}$ for each J_f and horizontal and vertical polarization. We see that for the same J_f, the values of $\tau_{(H,V)}^{J_f}$ are nearly the same, and there are never any crossings of $\tau_{(H,V)}^{J_f}$ for different J_f.

We can now compute a predicted optical depth in each of the two polarizations. We assign each line a Gaussian profile, given by some velocity width Δv. The normalization factors are all the same; they depend on the total column density of metastable helium atoms, which is not computed in this section. It could be taken by fitting to observations (here we set the peak optical depth to 0.05) or from a theory calculation

similar to Oklopčić & Hirata (2018). The result is

$$\tau(\lambda)_{(H,V)} = \sum_{J_f} Y \tau_{(H,V)}^{J_f} \exp\left\{-\frac{(\lambda - \lambda_{J_f})^2}{\Delta\lambda^2}\right\}, \qquad (27)$$

where $\Delta\lambda = (\Delta v/c)\lambda_0$, Δv is the velocity width,[10] λ_0 is 1083 nm, and Y is the normalization set by observations.

The total intensity and Stokes parameter Q are plotted as functions of wavelength in Figure 5. In the left panel of Figure 5, we see the absorption features in the spectrum relative to the out-of-transit signal (I_c). The weaker and bluer absorption feature is due to the transition from $2^3\mathrm{S}$ to $2^3\mathrm{P}_{J=0}$. The more prominent absorption feature is due to the transitions from $2^3\mathrm{S}$ to $2^3\mathrm{P}_{J=1,2}$. Since the $J = 1$ and $J = 2$ states are very close in energy, their absorption signals are blended; their combined oscillator strengths are a factor of 8 larger than the $J = 0$ transition, hence the deeper absorption feature. For the right panel in Figure 5, the Stokes parameter Q undergoes a continuous transition from positive (polarization perpendicular to the B-field) in the blue feature to negative (polarization parallel to the B-field) in the red feature. This positive–negative behavior had to happen, because in an $^3\mathrm{S}^e \rightarrow {}^3\mathrm{P}^o$ absorption the spin degree of freedom does not participate in the transition and the initial orbital state is isotropic; thus by sum rules the frequency-integrated cross section $\int \sigma(\nu)d\nu$ is the same for both incident photon polarizations regardless of how the atom is spin-polarized. This means that if one line has linear polarization, the other must have the opposite linear polarization, giving the shape of the curve in the right panel of Figure 5.

4. Numerical Calculation

We now turn to numerical calculations. We describe our use of the HAZEL code in Section 4.1, and then we proceed to consider a range of cases with a uniform magnetic field (including several orientations and strengths). We defer discussion of nonuniform fields and resulting suppression of the polarization signal to Section 5.1.

4.1. HAZEL Code

We use the publicly available code HAZEL (version 2.0),[11] developed by Asensio Ramos et al. (2008), to calculate the effect of a planetary magnetic field on the observed polarization of the helium 1083 nm line. HAZEL (*HAnle and ZEeman Light*) calculates the Stokes profiles of radiation passing through a constant-property slab of helium in the presence of a magnetic field.[12] The code takes into account all the relevant physical processes: optical pumping; atomic-level polarization; level crossing and repulsion; and the Hanle, Zeeman, and Paschen-Back effects. The helium model used in HAZEL includes transitions between the following atomic levels: $2s\ ^3\mathrm{S}$, $3s\ ^3\mathrm{S}$, $2p\ ^3\mathrm{P}$, $3s\ ^3\mathrm{P}$, and $3d\ ^3\mathrm{D}$.

A constant-property slab of neutral helium is assumed to be located at a distance h from the light source whose incident spectrum is modeled after the Sun. The slab's optical depth in
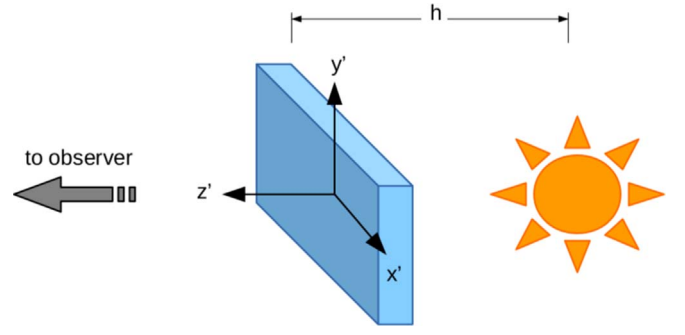

Figure 6. Problem setup for the HAZEL code used in our analysis: a constant-property slab of neutral helium is placed at a distance $h \sim 0.05$ au from a star with spectral properties of the Sun, along the z'-axis, which connects the star and the observer. A magnetic field characterized by (B_x', B_y', B_z') permeates the slab.

the red component of the helium line (τ) and the line width (Δv) are free parameters that determine the shape of the Stokes I profile. For our fiducial case, we choose the values of parameters that produce an absorption line similar to those observed in close-in exoplanets (e.g., Allart et al. 2018, 2019; Nortmann et al. 2018): $h \sim 0.05$ au, $\tau = 0.05$, and $\Delta v = 10.0$ km s^{-1}.

Our choice of the problem geometry is shown in Figure 6 (note that the coordinate system defined here is different from the one introduced in Section 2.2): the slab is located on the z'-axis, that is, the line of sight from the observer to the star. The magnetic field strengths along all three components of the coordinate system (B_x', B_y', B_z') are free parameters of the model. In the following sections, the magnetic field component parallel to the line of sight is denoted by $B_\parallel = B_{z'}$, and the component perpendicular to the line of sight is $B_\perp = \sqrt{B_{x'}^2 + B_{y'}^2}$.

4.2. Polarization in the Presence of a Longitudinal Magnetic Field

First we investigate the dependence of radiation polarization on the presence of a magnetic field along the line of sight. This component of the magnetic field induces circular polarization because of the longitudinal Zeeman effect: in an external magnetic field, atomic levels with total angular momentum J split into $(2J + 1)$ sublevels, with the splitting proportional to the magnetic field strength. The wavelength shifts between different components of the spectral line result in line polarization.

Figure 7 shows the radiation intensity (Stokes I) and circular polarization (Stokes V) calculated using the HAZEL code with the setup described in the previous section. We vary the strength of the magnetic field in the z' direction, while keeping all other parameters fixed. The middle panel shows the amplitude of the Stokes V parameter on a logarithmic scale, ranging from ∼few $\times 10^{-6}$ for $B_\parallel = 1$ G to ∼few $\times 10^{-3}$ for $B_\parallel = 1$ kG. The right panel shows the Stokes V line profile on a linear scale, consisting of a positive and a negative part in both the blue and red components of the helium 1083 nm line.

4.3. Polarization in the Presence of a Transverse Magnetic Field

Next we investigate the radiation polarization signal in the presence of a magnetic field perpendicular to the line of sight. This component of the magnetic field modifies the atomic-level

---

[10] We define this to be $\sqrt{2}$ times the standard deviation of the line-of-sight velocity; see Equation (5.43) of Landi Degl'Innocenti & Landolfi (2004). This is consistent with the input parameter to HAZEL.

[11] https://github.com/aasensio/hazel2

[12] HAZEL can also be used in "inversion mode" to infer model parameters from a set of observed Stokes parameters.
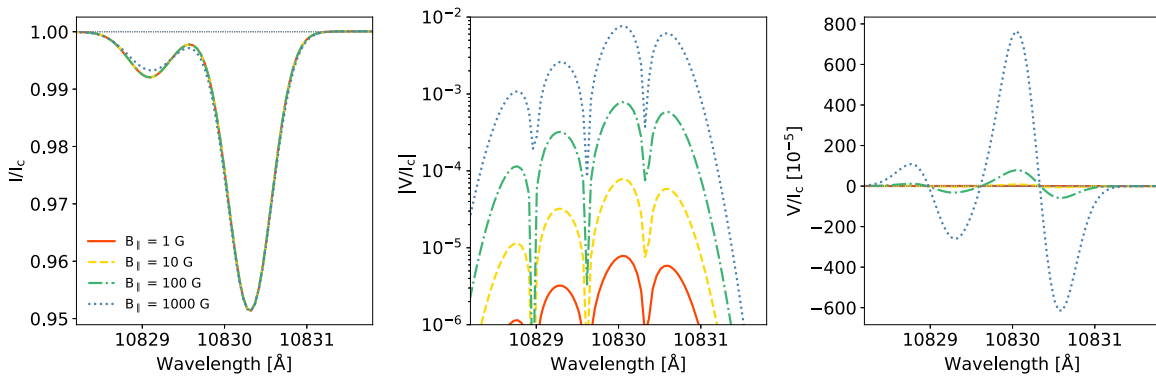
Figure 7. Magnetic field along the line of sight produces circular polarization in the helium 1083 nm line. The left panel shows the radiation intensity (Stokes I). The absorption line profile resembles those observed in transiting exoplanets. The middle panel shows the magnitude of the circular polarization signal (Stokes V). The full Stokes V profile is shown in the right panel.
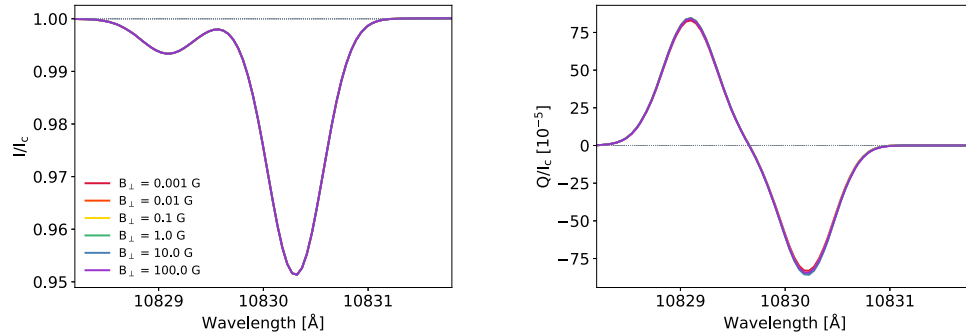

Figure 8. Transverse magnetic field produces a linear polarization signal that is independent of the magnetic field strength over many orders of magnitude. The left panel shows the radiation intensity, and the right panel shows the induced linear polarization (Stokes Q). In the optically thin case, the red and blue components of the helium 1083 nm triplet have the same magnitude of linear polarization, with opposite signs.

polarization induced by anisotropic radiation and creates linear polarization in the helium 1083 nm line through the Hanle effect (Trujillo Bueno et al. 2002). Figure 8 shows the linear polarization signal (Stokes Q) in the presence of $B_\perp$ of strength ranging from 0.001 G to 1 kG. Linear polarization is induced by the presence of a magnetic field perpendicular to the line of sight, but the polarization signal does not depend on the magnetic field strength in the analyzed range because it is in the "saturated Hanle regime." The amplitude of the linear polarization signal is on the order of 10^{-4}–10^{-3}, and the blue and red components of the helium 1083 nm line have opposite polarities of the same magnitude (in the optically thin case; see Section 4.5 for more details on the optically thick case). Note the excellent agreement between the HAZEL calculation in Figure 8 and the analytic calculation in Figure 5.

4.4. Polarization in the Presence of a Magnetic Field of Arbitrary Orientation

In the most general case, we consider a magnetic field with nonzero components in both the line-of-sight and perpendicular directions. We consider a range of $B_\perp$ between 0.1 and 100 G. The addition of a $B_\parallel$ (in this case $B_\parallel = 10$ G) breaks the degeneracy in the linear polarization signal and induces a circular polarization signal (see Figure 9). For $B_\perp \ll B_\parallel$, the linear polarization is significantly reduced compared to the $B_\parallel = 0$ case shown in Figure 8. For $B_\perp \gg B_\parallel$, the linear polarization signal remains virtually the same as in the $B_\parallel = 0$ case. This makes sense in the context of the analytic model (Section 3), because once the field is strong enough that the metastable helium atoms precess many times between

interactions ($B \gg B_I$), it is the direction rather than strength of the field that determines the mean polarization of the atoms. For $B_\perp \ll B_\parallel$, we are looking down the field ($\theta_\star \approx 0$).

On the other hand, the presence of a $B_\perp$ field has a less dramatic effect on the circular polarization signal, whose amplitude remains at the same level as in the $B_\perp = 0$ case, shown in Figure 7. This is because, while the Zeeman splitting is proportional to the total field B, the fractional circular polarization of each component (for $\Delta M_J = \pm 1$, i.e., the components that have circular polarization) is proportional to $\cos\theta_\star$; thus, when the Zeeman splitting is small compared to the line width ($B \ll B_{IV}$), the amplitude of the negative–positive pattern in Stokes V is proportional to $B\cos\theta_\star = B_\parallel$ (Seares 1913). However, for $B_\perp \gg B_\parallel$, the line profile changes so that the positive-V and the negative-V parts of both the blue and red components of the helium 1083 nm multiplet have roughly equal amplitudes.

4.5. Dependence on Optical Depth

In the previous examples, we kept the optical depth in the red component of the helium 1083 nm line fixed at $\tau = 0.05$. In Figure 10 we show how the polarization signal changes with changing the optical depth of the medium. In the optically thin regime, the polarization signal increases linearly with optical depth, with roughly equal polarization amplitudes in the blue and red components. As optical depth grows ($\tau \gtrsim 0.1$), the linear polarization amplitude in the red component becomes smaller than the linear polarization of the blue component.

Figure 11 shows the results for $\tau = 3$ in the red component of the line. This example is motivated by observations of the
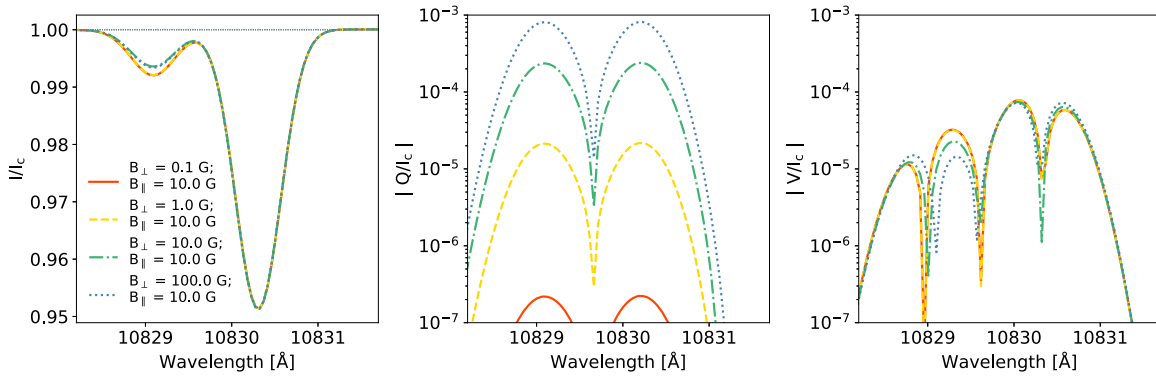
Figure 9. Magnetic field component along the line of sight ($B_\parallel$) breaks the degeneracy in the linear polarization signal induced by the perpendicular component ($B_\perp$).
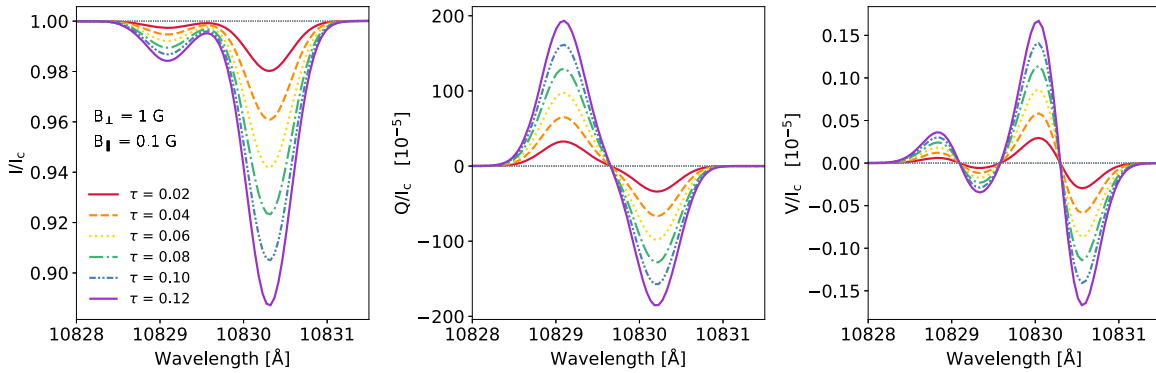

Figure 10. Radiation intensity (left), linear polarization (middle), and circular polarization (right) for different values of optical depth, with all other parameters fixed, including the magnetic field strength and orientation.

exoplanet HD 189733b (Salz et al. 2018), whose line profile has a low red-to-blue component ratio of ∼3:1 (the optically thin ratio is ∼8:1). The linear polarization signal in the optically thick red component gets significantly reduced in amplitude and its profile modified compared to the blue component, which is still in the optically thin regime.

5. Discussion

In this section, we examine the prospects for observing the calculated polarization at 1083 nm in transits of close-in exoplanets and discuss potential challenges for observations.

5.1. Combining Polarization Signals from Different Parts of the Atmosphere

Our results presented in the previous section were obtained for homogeneous slabs of helium permeated with uniform magnetic fields. In real observations, the signal would consist of contributions from different parts of the exoplanet atmosphere, characterized by different physical properties, including different geometries of the magnetic field. Magnetic fields in the atmospheres of highly irradiated, close-in exoplanets can have complex geometries; toroidal magnetic fields can be induced in the atmosphere by winds of ionized gas moving through the global, deep-seated, poloidal magnetic field (e.g., Rogers & Komacek 2014; Rogers & McElwaine 2017). Here we investigate the circumstances under which the polarization signals from different regions in the atmosphere can cancel each other out because of the differences in the magnetic field geometry.

We use HAZEL to calculate the polarization signals arising from two independent slabs. Initially, we set all properties of the two slabs to be equal, except the magnetic field orientation. We find that the polarization signals from the two slabs almost entirely cancel out if (1) the slabs have opposite magnetic fields along the line of sight ($B_{z,1} = -B_{z,2}$) and (2) if their magnetic field components perpendicular to the line of sight are equal in magnitude, but tilted by 90° with respect to each other (e.g., $B_{x,1} = -B_{y,2}$ and $B_{y,2} = B_{x,1}$). We show the results for one such example in Figure 12 ("fiducial" case, black line). If the entire atmosphere could be split pair-wise into regions that mutually cancel each other, such as these two slabs, the overall polarization signal from the planetary atmosphere would be below the detection limits of current spectropolarimetric instruments.

However, even small deviations in slab properties lead to detectable levels of linear polarization. Figure 12 shows the polarization signal in cases when different properties of one of the slabs have been altered by a small amount (10%–20%) relative to the fiducial case, thereby breaking the symmetry of the problem. Even such small deviations from symmetry produce linear polarization signals on the order of a few × 10^{-5}, which may be reached with upcoming instruments (see Section 5.2).

5.2. Observability of the Polarization Signal

The polarization signals we found in this paper are small—approximately 0.1% for a favorable field geometry and 0.01% and weaker signals for less favorable situations—but fortunately the target stars are bright, and high signal-to-noise ratio
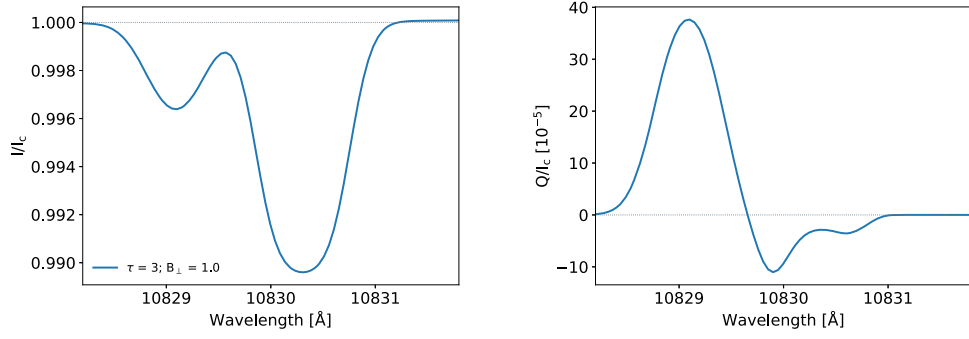
Figure 11. A slab of helium that is optically thick in the red component of the 1083 nm line produces a radiation intensity profile with a smaller red-to-blue line ratio compared to the optically thin case. For $\tau = 3$, we obtain the line ratio $\sim$3:1 (left panel), similar to that observed in HD 189733b (Salz et al. 2018). The right panel shows the reduced linear polarization in the optically thick red component of the helium line.
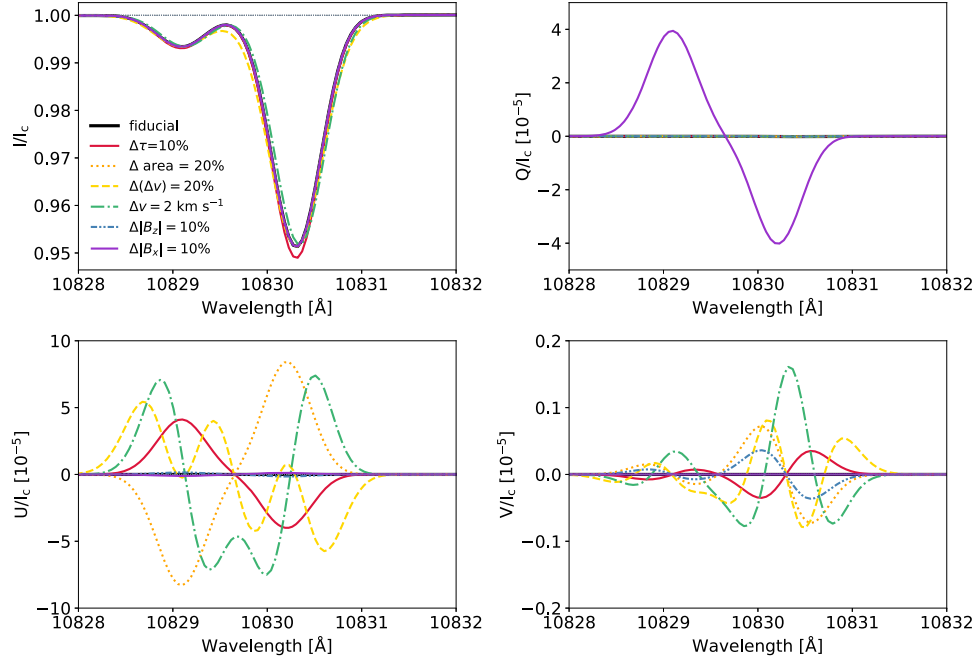

Figure 12. The fiducial case (black solid line) shows two slabs with identical properties (e.g., area, optical depth) and B-field orientation such that the polarization signals from the two slabs completely cancel each other out. Changing the slab properties even by a small amount, $\sim$10%–20%, induces a linear polarization signal $\gtrsim 10^{-5}$. Cancellation of the linear polarization signal below the observability threshold of 10^{-5}, arising from combining signals from different parts of a planetary atmosphere, hence seems unlikely.

(S/N) spectropolarimetry is possible. For spectropolarimetry dominated by source Poisson noise (the relevant regime here) and obtained by feeding the two polarization states through separate fibers to a spectrograph, the uncertainty in polarization is $\sigma(Q/I) = N_\gamma^{-1/2}$, where N_γ is the total number of photons per bin.[13] This is

$$\sigma(Q/I) = 0.001 \times 10^{0.2(m_{AB}-9.1)} \times \frac{3.6 \text{ m}}{D}$$
$$\times \left(\frac{0.023}{\eta} \frac{10 \text{ km s}^{-1}}{\Delta v} \frac{10^4 \text{ s}}{t_{obs}} \right)^{1/2}, \qquad (28)$$

where m_{AB} is the apparent AB magnitude of the star at $\sim$1.08 μm, D is the telescope diameter, η is the net throughput (including vignetting and fiber aperture losses), Δv is the bin width, and t_{obs} is the observation time. We have scaled the instrument parameters to the SPIRou[14] instrument on the Canada–France–Hawaii Telescope, and 10^4 s is a typical single transit duration. Two of the planets with large 1083 nm transit depth are WASP-107b (depth 5.5%; Allart et al. 2019) and WASP-69b (depth 3.6%; Nortmann et al. 2018); their host stars have $J_{AB} = 10.3$ and 8.9, respectively (Cutri et al. 2003). HAT-P-11b, HD 209458b, and HD 189733b have lower 1083 nm transit depths, but with host stars at $J_{AB} = 8.5$, 7.5, and 7.0, respectively, it should be possible to achieve smaller uncertainties on Q/I. All of these systems are in an appropriate decl. range for CFHT/SPIRou.

---

[13] Only one of the polarization Stokes parameters can be measured at a time, since this technique does not measure the correlation between the two polarization states. In an instrument such as SPIRou, the x and y polarizations are separated by a Wollaston prism, and rotatable quarter-wave transformers are used to map the desired Stokes parameter from the sky into Stokes Q as seen by the prism (Parès et al. 2012).
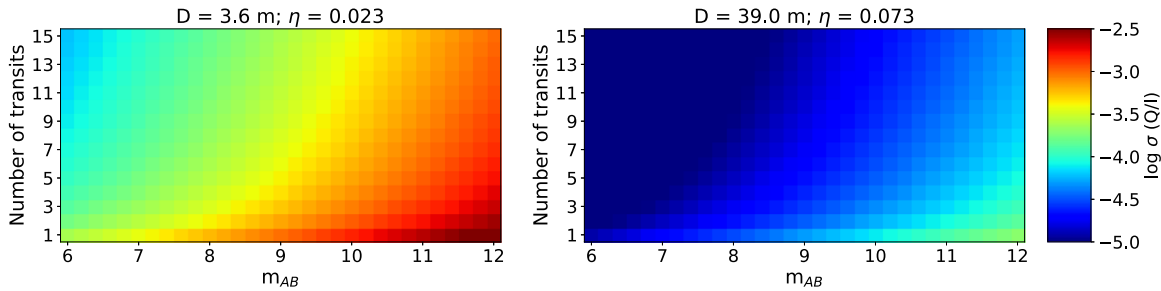
[14] http://etc.cfht.hawaii.edu/spi/

Figure 13. Uncertainty in the polarization signal Equation (28) as a function of the total exposure time (shown as the number of combined transit observations, assuming one transit lasts 10^4 s) and the magnitude of the host star. The left (right) panel shows the results for a telescope diameter of 3.6 (39.0) m and the instrument throughput of 0.023 (0.073), based on the corresponding values for CFHT/SPIRou (ELT/HIRES). In order to detect the polarization signal described in this work, the required uncertainty should be $\lesssim 10^{-4}$ (turquoise and blue regions). Note that this is for measurement of one polarization Stokes parameter; measurement of both Q and U to the same precision would require twice as many transits.

With multiple transits[15] (see Figure 13, left panel), and if systematics associated with calibration and stellar variability can be addressed, SPIRou should enable initial exploration of the interesting parameter space for He I line polarization. However, if one wants to be able to detect less favorable field geometries or measure the transit phase or velocity dependence of the polarization, a future spectropolarimeter with more light-gathering capability will be required. Some improvements may be realized by optimizing materials and coatings for the $Y + J$ bands (SPIRou achieves a factor of a few higher throughput in $H + K$). The biggest improvement would be to go to a larger telescope. We take as an example the ELT-HIRES instrument concept (Marconi et al. 2018) for the Extremely Large Telescope (ELT), $D = 39$ m, and based on available information we set $\eta = 0.073$.[16] A polarimetric mode, based on selection and splitting of the polarizations at intermediate focus, has been proposed (Di Varano et al. 2018). This would represent a factor of ~ 20 improvement in polarization sensitivity relative to SPIRou, and in principle fractional polarizations Q/I down to a few $\times\ 10^{-5}$ would be accessible (see Figure 13, right panel).

5.3. Other Sources of In-transit Polarization

Linear polarization signals can arise during exoplanet transits from other sources, but they should not interfere with the measurements we are proposing in this study. The proposed method—high-resolution transmission spectropolarimetry—is differential in terms of both time and wavelength dependence. In other words, we propose to measure the change in polarization in-transit versus out-of-transit, as well as in the helium line versus the continuum. Therefore, any source of constant or broadband polarization should be removed in the process automatically. However, it may still contribute to the noise, which is why it is important to note that the continuum linear polarization signal of transiting exoplanets is expected to be much smaller than the signals predicted in this study.

Measuring the broadband linear polarization signal during transits of exoplanets has been proposed as a method for detecting and characterizing transiting exoplanets (e.g., Carciofi & Magalhães 2005; Kostogryz et al. 2015). Searches for these signals have been conducted in recent years, without confirmed detections so far (Berdyugina et al. 2008; Wiktorowicz 2009; Bott et al. 2016, 2018). Broadband linear polarization results from radiation scattering in the stellar atmosphere. For a spherically symmetric star, the signals integrated over the entire stellar disk cancel out; however, a transiting exoplanet breaks the symmetry of the star as seen by the observer, which results in net polarization. The expected linear polarization signal is on the order of a few $\times\ 10^{-6}$ at short wavelengths around 450 nm (Kostogryz et al. 2015, 2017). Due to the strong wavelength dependence of Rayleigh scattering, the amplitude of the polarization signal drops significantly at longer wavelengths and is expected to be negligible at 1083 nm.

Potentially more significant sources of contamination are the intrinsic stellar variability and stellar-disk inhomogeneity in the helium triplet polarization that are due to stellar activity. The potential impact of intrinsic stellar variability in the helium line at short timescales relevant for transit observations (a few hours) is still an open question in the context of radiation intensity, and even more so in terms of radiation polarization. Because areas of intense chromospheric absorption in the helium line are associated with active regions, and are thus unevenly distributed across the stellar disk, it is possible that a transiting planet could induce a change in the observed helium line just by occulting an exceptionally active or inactive part of the stellar disk.

Initial analyses suggest that the contamination of transmission spectra by stellar activity at 1083 nm is not very severe and should not impede observations of extended exoplanet atmospheres, at least when it comes to radiation intensity. Repeated transit observations of exoplanets at 1083 nm show consistent transit depths and similar light curves over periods of months and years, indicating that the effects of stellar activity and variability do not dominate the signal. Furthermore, by simulating exoplanet transits using synthetic spectra of F- and G-type stars with different levels of stellar activity, as well as the publicly available solar data, Cauley et al. (2018) found that the contrast between active and inactive regions at 1083 nm is small and should not result in significant contamination of helium transmission spectra. Similar investigations of the impact of stellar activity on transmission polarimetry at 1083 nm are needed, and important initial insights could be

---

[15] Here we assume that the planets are tidally locked, which should be a valid assumption for most close-in exoplanets. Therefore, the magnetic field geometry relative to the observer is expected to be similar (but possibly not identical if it depends on stellar activity) in successive transits, which should allow combining signals from multiple transit observations.

[16] We estimated the throughput from the online exposure time calculator for intensity mode (http://www.arcetri.inaf.it/~hires/etc.html). The value of 0.073 was set to reproduce the correct S/N ratio, although it is very close to the 0.075 that one gets by multiplying the exposure time calculator input parameters because we are very source Poisson dominated.

provided by studies of the spatially resolved polarization of the Sun.

6. Summary

We propose a method for directly detecting the presence of magnetic fields in the atmospheres of transiting exoplanets. The method, similar to the method originally introduced by solar physicists (see Trujillo Bueno et al. 2002), is based on detecting radiation polarization in the helium line triplet at 1083 nm during transits of close-in exoplanets with extended or escaping atmospheres. Using analytic and numerical calculations, we demonstrated that the presence of a transverse magnetic field induces a linear polarization signal on the order of 10^{-4}–10^{-3}. A broad range of magnetic field strengths, including those measured for most planets in the solar system, can result in a polarization signal of this magnitude. Therefore, this method is extremely sensitive to the presence of magnetic fields in exoplanet atmospheres. Assessing the magnetic field strength, however, may be challenging in this saturated Hanle regime, unless the field strength is high enough to induce a detectable level of circular polarization, due to the longitudinal Zeeman effect. Detecting the calculated polarization signals could be achieved with future high-resolution near-infrared spectropolarimeters on large ground-based telescopes, or even with current facilities (such as SPIRou on CFHT) if multiple transit observations of the same target were combined.

Appendix
Gas Densities Required for Depolarizing Collisions

The cross section for elastic spin-exchange (i.e., depolarizing) electron-metastable helium collisions for electron energies around 0.5 eV (typical for temperatures of $\sim 10^3$–10^4 K) is $\sigma \sim 100$ Å$^2 \sim 10^{-14}$ cm^2 (Sklarew & Callaway 1968). The rate at which an electron of that energy collides with a helium atom in the metastable state, per unit volume, is therefore $R = \sigma \times \sqrt{2E/m_e} \sim 7 \times 10^{-7}$ cm^3 s^{-1}. Collisions of metastable helium atoms with electrons and hydrogen atoms that cause triplet-to-singlet transitions have even lower average rates (given in Oklopčić & Hirata 2018, Section 3.3). Therefore, in order for the total collision rate $n_e \times R$ to be above the scattering rate of the 1083 nm photons (at 0.05 au
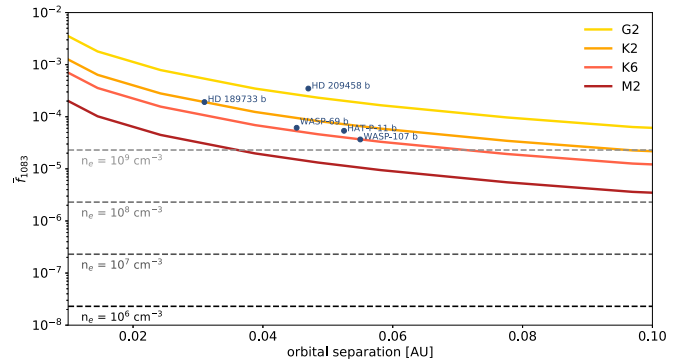

Figure 14. Solid lines show the phase space density of 1083 nm photons, $\overline{f}_{1083}$, as a function of orbital distance around stars of spectral types G2 to M2. Dashed lines show thresholds below which depolarizing collisions can destroy atomic polarization, assuming a certain electron number density in a planetary atmosphere, n_e. Planets in which the helium 1083 nm absorption has been detected occupy the part of the parameter space in which depolarizing collisions do not play the dominant role, which is why we did not take them into account in our calculation.

from a Sun-like star) of $3A_{ul}\overline{f}_{1083} = 3 \times 10^7 \times 10^{-4}$ s^{-1}, the electron number density, n_e, must exceed 4×10^9 cm^{-3}.

It is also possible to have elastic spin-exchange collisions between metastable helium and neutral hydrogen atoms (H I) because the hydrogen atom has net electron spin. We were not able to find a published rate coefficient, but we do note that spin exchange only occurs when the He 2s and H 1s orbitals overlap each other and hence give rise to a nonzero exchange integral. Because the He 2s orbital has a wave function that declines with an ~ 1 Å exponential scale length, we expect the cross section at which this interaction becomes important to be of order 10 Å$^2 \sim 10^{-15}$ cm^2. This would makes the He 2^3S + H I spin exchange negligible compared to He 2^3S + e^-, since the cross section is 10 times smaller and v is 40 times smaller (because of the reduced mass); thus only when the ionization fraction drops below $\sim 1/(10 \times 40) \sim 0.0025$ would H I collisions dominate.

According to hydrodynamic simulations of escaping exoplanet atmospheres (e.g., Salz et al. 2016), total gas densities of $\sim 10^{10}$ cm^{-3} are expected at altitudes below ~ 1.1–1.2 R_{pl}, where most of the gas is neutral and electron collisions become further suppressed by the low ionization fraction ($\lesssim 10^{-2}$). Furthermore, observations of helium signals from exoplanets made so far indicate that the helium absorption arises in atmospheric layers extending out to much higher altitudes, up to ~ 2–3 R_{pl} (Allart et al. 2018; Nortmann et al. 2018). The expected gas densities at these high altitudes are between 10^6 and 10^9 cm^{-3} (Salz et al. 2016; with lower densities being more representative of larger planets, which are more favorable for transit observations). Because most hydrogen atoms in this region are expected to be ionized, the number density of free electrons is roughly of the same order. Hence, in most cases of interest, depolarizing electron collisions should not be able to destroy the lower-level polarization of helium atoms in these upper atmospheric layers.

However, for planets around stars of later spectral types than the Sun, the flux of 1083 nm photons at the same orbital distance can be significantly smaller. In Figure 14, we show the phase space density of 1083 nm photons as a function of a planet's orbital separation for different late-type stars. The yellow curve, representing the Sun, is obtained from HAZEL, whereas the other lines are proportionally scaled down, based

on the observed flux density in the continuum near the 1083 nm line of stars of given spectral type in the MUSCLES survey (France et al. 2016). Specifically, the K2 curve is modeled after ϵ Eri, K6 is based on HD 85512, and M2.5 on GJ 176. Dashed lines indicate the levels of irradiation at which the rate of scattering of 1083 nm photons becomes comparable to the rate of depolarizing collisions, at a given electron number density, according to the above-described calculation. In other words, regions of parameter space in which the solid lines lie above the dashed lines are favorable for using the Hanle effect as a probe of magnetic fields in exoplanets. This technique can only be applied up to a certain orbital distance from the host star, and this limiting distance is smaller for cooler stars and for planetary atmospheres of higher densities. As shown in Figure 14, exoplanets with reported detections of helium (indicated by blue dots) all lie well within the favorable part of the parameter space, for the expected electron densities of $n_e \sim 10^6$–10^9 cm^{-3}.

ORCID iDs

Antonija Oklopčić ⓘ https://orcid.org/0000-0002-9584-6476
Makana Silva ⓘ https://orcid.org/0000-0002-1717-4424
Paulo Montero-Camacho ⓘ https://orcid.org/0000-0002-6998-6678
Christopher M. Hirata ⓘ https://orcid.org/0000-0002-2951-4932

References

Allart, R., Bourrier, V., Lovis, C., et al. 2018, Sci, 362, 1384
Allart, R., Bourrier, V., Lovis, C., et al. 2019, A&A, 623, A58
Alonso-Floriano, F. J., Snellen, I. A. G., Czesla, S., et al. 2019, A&A, 629, A110
Asensio Ramos, A., Trujillo Bueno, J., & Land i Degl'Innocenti, E. 2008, ApJ, 683, 542
Barrat, J. P., & Cohen-Tannoudji, C. 1961, J. Phys. Radium, 22, 329
Berdyugina, S. V., Berdyugin, A. V., Fluri, D. M., & Piirola, V. 2008, ApJL, 673, L83
Bott, K., Bailey, J., Cotton, D. V., et al. 2018, AJ, 156, 293
Bott, K., Bailey, J., Kedziora-Chudczer, L., et al. 2016, MNRAS, 459, L109
Carciofi, A. C., & Magalhães, A. M. 2005, ApJ, 635, 570
Cauley, P. W., Kuckein, C., Redfield, S., et al. 2018, AJ, 156, 189
Cauley, P. W., Shkolnik, E. L., Llama, J., & Lanza, A. F. 2019, NatAs, 3, 1128
Cutri, R. M., Skrutskie, M. F., van Dyk, S., et al. 2003, yCat, II/246
Di Varano, I., Woche, M., Strassmeier, K. G., et al. 2018, Proc. SPIE, 10706, 107061Y
Donati, J. F., & Landstreet, J. D. 2009, ARA&A, 47, 333
Edmonds, A. R. 1960, Angular Momentum in Quantum Mechanics (Princeton, NJ: Princeton Univ. Press)
France, K., Parke Loyd, R. O., Youngblood, A., et al. 2016, ApJ, 820, 89
Hale, G. E. 1908, ApJ, 28, 315
Hallinan, G., Antonova, A., Doyle, J. G., et al. 2008, ApJ, 684, 644
Hanle, W. 1924, ZPhy, 30, 93
Hunter, J. D. 2007, CSE, 9, 90
Jones, E., Oliphant, T., & Peterson, P. 2001, SciPy: Open Source Scientific Tools for Python, http://www.scipy.org/
Kao, M. M., Hallinan, G., Pineda, J. S., Stevenson, D., & Burgasser, A. 2018, ApJS, 237, 25
Kostogryz, N. M., Yakobchuk, T. M., & Berdyugina, S. V. 2015, ApJ, 806, 97
Kostogryz, N. M., Yakobchuk, T. M., Berdyugina, S. V., & Milic, I. 2017, A&A, 601, A6
Kramida, A., Ralchenko, Y., Reader, J. & NIST ASD Team 2018, NIST Atomic Spectra Database v5.6.1, https://physics.nist.gov/asd
Landi Degl'Innocenti, E., & Landolfi, M. 2004, Polarization in Spectral Lines (Dordrecht: Kluwer)
Lazio, J., Hallinan, G., Airapetian, V., et al. 2018, arXiv:1803.06487
Leroy, J. L., Ratier, G., & Bommier, V. 1977, A&A, 54, 811
Marconi, A., Allende Prieto, C., Amado, P. J., et al. 2018, Proc. SPIE, 10702, 107021Y
Morin, J., Donati, J. F., Petit, P., et al. 2010, MNRAS, 407, 2269
Murphy, T., Bell, M. E., Kaplan, D. L., et al. 2015, MNRAS, 446, 2560
Nortmann, L., Pallé, E., Salz, M., et al. 2018, Sci, 362, 1388
Oklopčić, A. 2019, arXiv:1903.02576
Oklopčić, A., & Hirata, C. M. 2018, ApJL, 855, L11
Oliphant, T. 2006, A Guide to NumPy (USA: Trelgol Publishing)
Parès, L., Donati, J. F., Dupieux, M., et al. 2012, Proc. SPIE, 8446, 84462E
Reiners, A., & Basri, G. 2007, ApJ, 656, 1121
Rogers, T. M., & Komacek, T. D. 2014, ApJ, 794, 132
Rogers, T. M., & McElwaine, J. N. 2017, ApJL, 841, L26
Rybicki, G. B., & Lightman, A. P. 1979, Radiative Processes in Astrophysics (New York: Wiley-Interscience)
Salz, M., Czesla, S., Schneider, P. C., et al. 2018, A&A, 620, A97
Salz, M., Czesla, S., Schneider, P. C., & Schmitt, J. H. M. M. 2016, A&A, 586, A75
Schubert, G., & Soderlund, K. M. 2011, PEPI, 187, 92
Seares, F. H. 1913, ApJ, 38, 99
Sklarew, R. C., & Callaway, J. 1968, PhRv, 175, 103
Spake, J. J., Sing, D. K., Evans, T. M., et al. 2018, Natur, 557, 68
Stenflo, J. O., Keller, C. U., & Gandorfer, A. 1998, A&A, 329, 319
Trujillo Bueno, J., & Asensio Ramos, A. 2007, ApJ, 655, 642
Trujillo Bueno, J., & Landi Degl'Innocenti, E. 1997, ApJL, 482, L183
Trujillo Bueno, J., Landi Degl'Innocenti, E., Collados, M., Merenda, L., & Manso Sainz, R. 2002, Natur, 415, 403
Trujillo Bueno, J., Merenda, L., Centeno, R., Collados, M., & Landi Degl'Innocenti, E. 2005, ApJL, 619, L191
Venumadhav, T., Oklopčić, A., Gluscevic, V., Mishra, A., & Hirata, C. M. 2017, PhRvD, 95, 083010
Wiktorowicz, S. J. 2009, ApJ, 696, 1116